The Astrophysical Journal, 891:122 (11pp), 2020 March 10 https://doi.org/10.3847/1538-4357/ab7340

Asymmetries and Broadenings of Spectral Lines in Strongly Charged Iron Produced during Solar Flares

Revati S. Mandage and Stephen J. Bradshaw
Department of Physics and Astronomy, Rice University, Houston, TX 77005, USA; rm61@rice.edu, stephen.bradshaw@rice.edu
Received 2020 January 3; revised 2020 February 3; accepted 2020 February 4; published 2020 March 12

Abstract

Spatially resolved spectroscopic observations show wing enhancements and broadening in extreme ultraviolet emission lines, particularly in hot iron lines. Various explanations ranging from plasma turbulence and magnetic perturbations, to nonthermal ion populations and multiple flows in unresolved structures have been proposed. In this work, we revisit the role of single loop plasma dynamics in spectral line shape by reproducing the wing enhancements of Fe XXIII and XXIV observed during a C-class solar flare using a single loop hydrodynamic model. We also run simulations with different loop lengths and the same beam parameters to investigate the role of loop length in line broadening and asymmetry. We find that the single loop model successfully reproduces line asymmetries and the loop length plays an important role in explaining some of the key observations such as the positive correlation between the Doppler shifts and line width, and broad but symmetric hot Fe lines.

Unified Astronomy Thesaurus concepts: Solar flares (1496); Solar activity (1475); Solar flare spectra (1982)

1. Introduction

Extreme ultraviolet emission (EUV) lines offer a closer look into the plasma dynamics and composition during solar flares. Intensities of spectral lines give information on the electron/ion densities as well as temperature of the flaring plasma, whereas the Doppler shifts in the lines arise due to bulk motion of the emitting ions (see Milligan 2015). An important feature of a spectral line is its shape, which is normally described by a Voigt function. The Voigt function is a convolution of a Lorentzian (intrinsic broadening in a line due to uncertainties in the energy levels), and a Gaussian (thermal broadening due to thermal motion of ions as well as instrumental broadening). However, we often see deviations from Voigt profiles in the form of wing enhancement and excess broadening in EUV lines observed from flaring active regions (Mason et al. 1986; Dere et al. 1989; Doschek et al. 1996, 2014, 2015; Imada et al. 2008; Milligan & Dennis 2009; Polito et al. 2017) and from nonflaring active regions (Hara et al. 2006; Doschek et al. 2007; Bryans et al. 2010; Peter 2010).

Random plasma motions due to turbulence along the line of sight have been considered to explain the excess broadening in spectral lines (Doschek et al. 1979; Antonucci et al. 1986; Alexander 1990; Larosa & Moore 1993). However, spatially resolved spectroscopy performed using the Coronal Diagnostic Spectrometer/*Solar and Heliospheric Observatory* (Harrison et al. 1995) and the EUV Imaging Spectrometer (EIS/*Hinode*; Culhane et al. 2007), and recently the *Interface Region Imaging Spectrograph* (*IRIS*; De Pontieu et al. 2014), has revealed some interesting trends that suggest possible reasons behind the excess broadening as well as wing enhancements in spectral lines. Imada et al. (2008) noted that the asymmetric line profiles were preferentially observed in new flare loops, indicating the role of plasma bulk flows resulting from chromospheric ablation during the impulsive phase. Pontieu et al. (2009) found similar upflow velocities from the blueshifted component in asymmetric lines across a wide range of temperature and magnetic field configurations, and proposed type II spicules to be the cause of the asymmetries in spectral lines. Peter (2010) observed that the line width for both core and minor components of asymmetric lines increases from the foot-points to the loop top and suggested the possibility of Alfvenic perturbations causing asymmetry in the broadening mechanism (see also Fletcher & Hudson 2008). Jeffrey et al. (2016, 2017) and Polito et al. (2018) suggested that the excess broadening may be caused by a flare-accelerated nonthermal ion population with non-Gaussian (e.g., κ) velocity distributions. It is also plausible that the excess broadening is due to the ion populations emitting in much hotter plasma far from their equilibrium formation temperatures (De Jager 1985; Bradshaw et al. 2004).

The high temperature line profiles ($\geqslant$10 MK) have been observed to show asymmetry with a strongly blueshifted ($\sim$200 km s^{-1}) component and a dominant stationary component (Milligan & Dennis 2009; Li & Ding 2011) while in other cases completely blueshifted and very broad lines have been seen (Brosius 2003; Watanabe et al. 2010; Zanna et al. 2011; Young et al. 2013; Tian et al. 2014; Graham & Cauzzi 2015; Polito et al. 2016) including the Fe XXI line observed by *IRIS* (Battaglia et al. 2015; Polito et al. 2015; Young et al. 2015; Dudík et al. 2016). Several studies have found a positive correlation between the Doppler velocity and nonthermal velocity (calculated from excess broadening) suggesting that the asymmetry as well as broadening in spectral lines may arise due to the presence of multiple flows in unresolved structures (Doschek et al. 1986, 2008; Hara et al. 2006; Bryans et al. 2010; Milligan 2011).

Numerical modeling offers a way to test these hypotheses and assess their applicability in various situations. To explain the asymmetric spectral lines observed in the nonflaring atmosphere Patsourakos & Klimchuk (2006) use a nanoflare model where thousands of unresolved strands are heated impulsively at different times. A snapshot of emission from these threads is approximated by taking the time average of a single strand over a few thousand seconds. They show that the resultant line profile is nonthermally broadened and can have a wing enhancement depending on the properties of the nanoflare. In a recent study, Polito et al. (2019) model the hot Fe XXI spectral line observed in a flare using different

multithread models that consist of about 100 threads of the same length and different inclination angles (with respect to the line of sight). They find that broader profiles are consistently asymmetric, and conclude that the superposition of flows alone cannot explain the observed broad and symmetric profiles, and consequently other nonthermal processes such as turbulence and/or magnetic perturbations are necessary to explain the observations. Both these works investigate the role of multiple flows in explaining line broadening and asymmetries. In the present work we show that the line asymmetries (blue-wing enhancements) observed during a flare can be reproduced through plasma dynamics in a single strand. We also demonstrate how loop length affects broadening and wing enhancement. In particular, we show that the hot Fe lines that are broad can both be symmetric and asymmetric depending on the model parameters. Section 2 describes the numerical experiments that are designed to reproduce the observed spectra and the numerical methods used. Section 3 discusses the results. The conclusions are presented in Section 4.

2. Numerical Experiments

Blue-wing enhancements in hot Fe lines, Fe XXIII and XXIV, were observed in a study by Milligan & Dennis (2009). We model this flare using their *RHESSI*-derived beam parameters by running field-aligned hydrodynamic simulations. Thirty-five different simulations are designed to span the range of uncertainties in the energy flux (F) and the low energy cutoff (E_C): $F = [5, 6, 7, 8, 9, 10, 11] \times 10^{10}$ erg cm^{-2} s^{-1}, $E_C = [11, 12, 13, 14, 15]$ keV. As the uncertainty in the power index (δ) is not high (± 0.7) and changing δ does not appreciably change the plasma dynamics (Reep et al. 2013), we keep it the same ($=7.6$) in all 35 cases. These beam parameters are held constant in time and the beam is operated for the entire duration of the impulsive phase (360 s) as deduced from the *GOES* light curves for this flare. The length of the loop is inferred from the *Transition Region and Coronal Explorer* image of the two bright points (Figure 1 of Milligan & Dennis 2009). By taking these two bright points as coronal foot-points of the loop, and the distance between them as the diameter of a semicircular loop, the total loop length (which includes 2.2 Mm deep chromospheres at both ends of the loop) was estimated to be 10.7 Mm. To study the role of loop length on line broadening and asymmetry, we run five simulations with loop lengths $2L = [10.7, 15, 20, 30, 50]$ Mm and beam parameters chosen randomly from the above 35 sets of the beam parameters: $F = 5 \times 10^{10}$ erg cm^{-2} s^{-1}, $E_C = 12$ keV, and $\delta = 7.6$ for each thread.

The hydrodynamic simulations are run using HYDRAD, which has been used for a large number of flare studies and predicts the evolution of a multispecies plasma (electrons, ions, and neutrals) responding to an injected electron beam, along the full length of a flaring loop, accounting for changes in the magnetic field strength and geometry, using adaptive grids to capture spatial scales of order a thousand kilometers to just a few meters (and less), and timescales of a few billionths of a second (Bradshaw & Cargill 2013; Reep et al. 2019).

HYDRAD solves for the bulk transport (with shock capturing), thermal conduction (accounting for flux saturation), viscous interactions, gravitational energy, Coulomb collisions, heating, and optically thick radiation in the lower atmosphere transitioning to optically thin radiation (lines and continuum) in the overlying atmosphere. HYDRAD also solves the time dependent equations which describe the evolution of the ionization state of the radiating elements. Optical depth effects in the lower solar atmosphere are treated by adopting the Vernazza, Avrett, and Loese (Vernazza et al. 1981) model C chromosphere and a prescription for optically thick radiative processes developed by Carlsson & Leenaarts (2012). In regions where the plasma is partially ionized the ionization and recombination of hydrogen, and the contribution of H I to energy transport by thermal conduction (Orrall & Zirker 1961), are included in the energy equations solved by HYDRAD.

The output from hydrodynamic simulations in terms of physical parameters is used to synthesize line-of-sight integrated spectra using a spectral synthesis code (Bradshaw & Klimchuk 2011; Reep et al. 2013, 2016). Nonequilibrium ionization is used to calculate ion populations (Bradshaw 2009). The spectra for 15 ions (He II, O VI, Mg VI, Mg VII, Fe VIII, Fe X, Fe XI, Fe XII, Fe XIII, Fe XIV, Fe XV, Fe XVI, Fe XVII, Fe XXIII, and Fe XXIV) that span the temperature range 0.05–16 MK as given by Table 1 of Milligan & Dennis (2009), taking into account the response function for *Hinode*/EIS, are synthesized by integrating the line intensities over 10 s (the exposure time of EIS used for their observations). The methodology used to predict the spectral line profiles is described in detail in Klimchuk & Bradshaw (2014) and Bradshaw & Klimchuk (2015).

3. Results and Discussion

Figures 1 and 2 show the Fe XXIII and Fe XXIV spectral line profiles for three representative runs with the beam parameters $F = [5, 8, 11] \times 10^{10}$ erg cm^{-2} s^{-1}, $E_C = [11, 15, 15]$ keV (Runs 1, 20, and 35 respectively). To compare the spectral line shape in each case, the spectra are normalized to intensity 1. The spectral profiles are plotted during four different time intervals within the first 25 s of flare evolution. In both cases we see that the spectral line shape evolves from Gaussian to red-wing-enhanced to blue-wing-enhanced to Gaussian (and stays Gaussian for the rest of the time over which the beam is operated).

It is important to note that out of 15 spectral lines, the blue-wing enhancement is seen only for Fe XXIII and XXIV both in the observations by Milligan & Dennis (2009) as well as in our simulations. Hence a question that naturally arises is why we observe blue-wing enhancements only in the very hot Fe lines but not in the remaining 13 lines. The explanation lies in the location over which these ions are formed. The effect of the changes in the plasma bulk-flow velocity at different locations will be reflected in the line shape when the ions are formed or exist at those locations. But if the ion population is more localized in a certain region, then the changes in the plasma bulk speed in other regions along the loop will not affect the line shape. The formation temperatures for Fe XXIII and XXIV are well above 10 MK, whereas the formation temperatures for the remaining 13 lines are much lower than 5 MK. We know from hydrodynamic simulations that as the beam begins to heat the loop, the transition region is pushed further down and most of the rest of the loop loop maintains uniformly high temperature due to efficient thermal conduction. This results in spatially extended Fe XXIII and XXIV populations along the loop, whereas populations of the other ions stay more localized in the TR and lower part of the loop. Plasma bulk flows in the loop carry these ions up along the loop, but since the temperature is extremely far from the peak formation

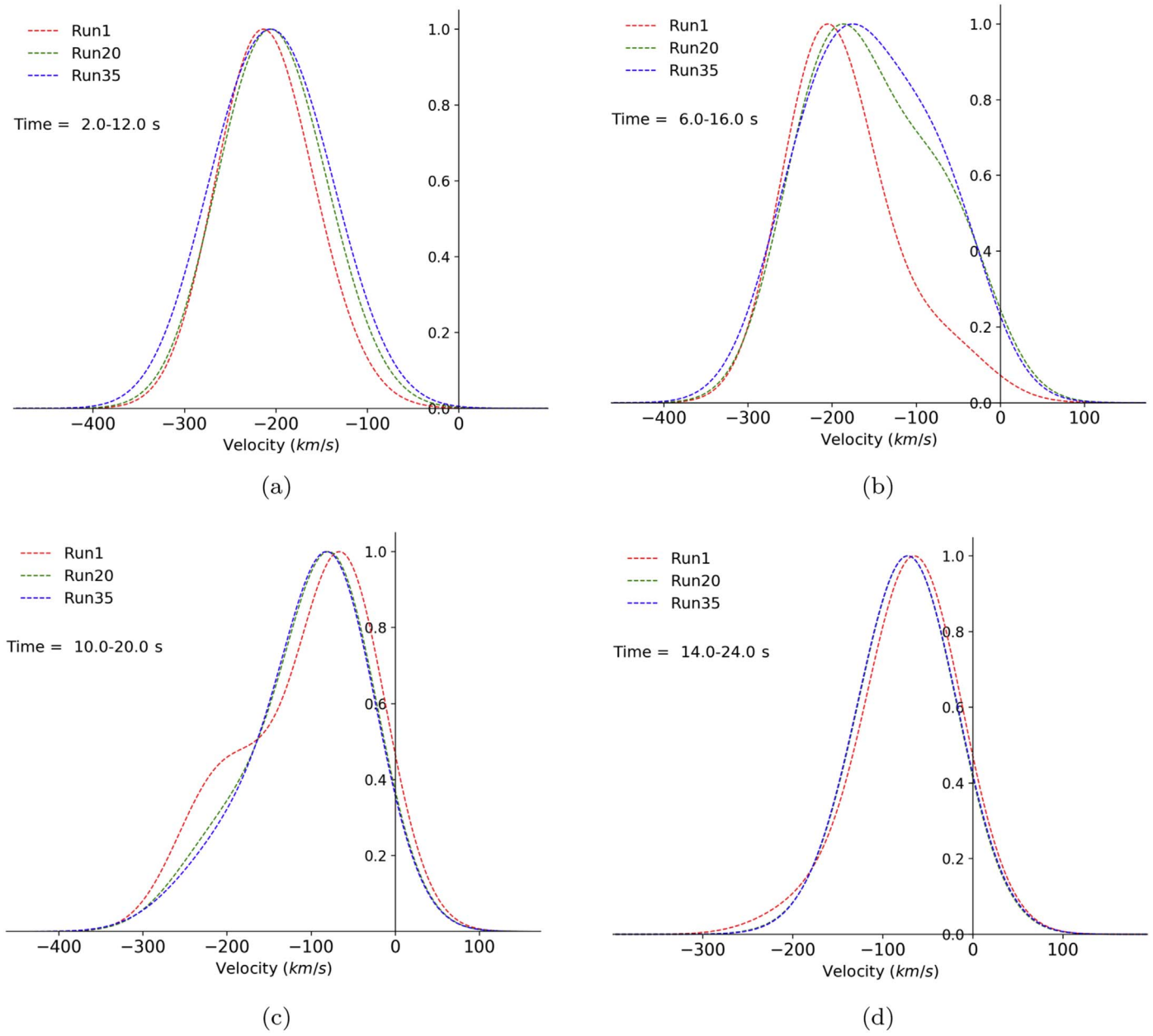

Figure 1. Spectral line profiles for Fe XXIII for Runs 1, 20, and 35 calculated at one of the foot-points of the loop. The intensities are normalized for individual spectra with respect to corresponding maximum intensities. Negative values indicate upward velocity/blueshift.

temperatures, their populations higher up the loop diminish very quickly. As a result, we have Fe XXIII and XXIV ion populations along most of the coronal part, whereas the other ion populations become quite localized at the foot-point of the loop.

Figure 3 offers a detailed explanation for the Fe XXIII spectral line profiles. The beam energy deposited in the chromosphere locally increases the plasma pressure which then drives up- and downflows along the loop. This results in the material front that moves upward toward the apex (see the top panel of Figure 3(a)). As the advection carries more material upward and the heating increases the temperature, the ion populations of the hot Fe ions track the material front. This enhances the population of Fe XXIII in the upper part of the loop (Figures 3(a) and (b)). Once the material front reaches the apex, it collides with the material front from the other side, and the plasma bulk velocity falls as they rebound. Hence the amount of material advected into the upper region of the loop begins to decrease. Additionally, the continued heating raises the upper region above the equilibrium formation temperatures while gradually increasing the temperature in the lower region of the loop to the ion formation temperatures. Due to this the ion populations increase quite rapidly and become localized in the lower part of the loop (Figures 3(c) and (d)).

Figure 1(a), where the spectrum for each case is a totally blueshifted Gaussian, is the result of emission from the high velocity, upper-region ions since during this interval the low velocity ion population at the foot-point region of the loop is small (compare Figures 3(a) and (c)). The low velocity, lower region ion population starts to increase (Figure 3(c)) which results in the red-wing enhancement seen in Figure 1(b). This low velocity population continues to increase, as the plasma

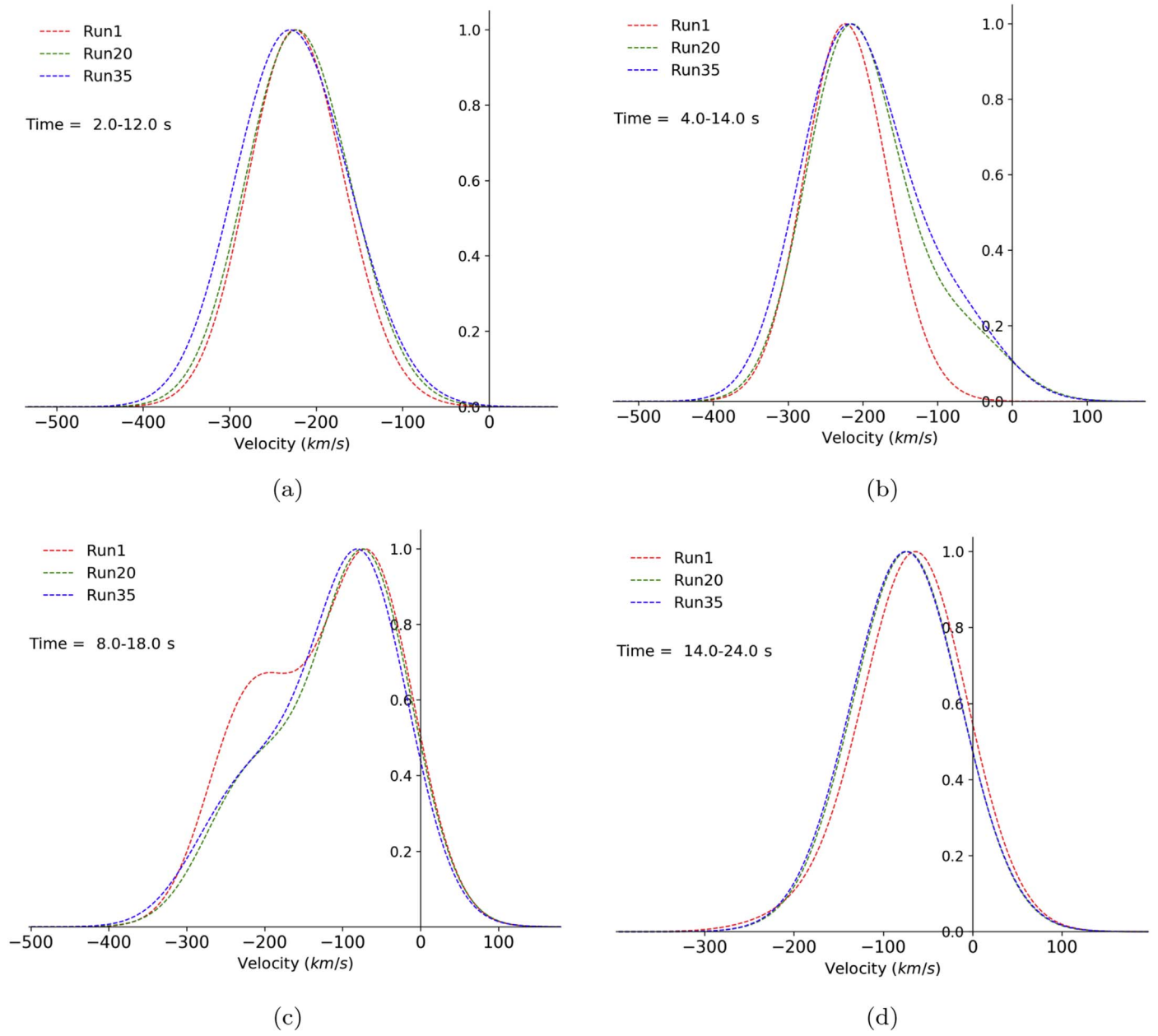

Figure 2. Spectral line profiles for Fe XXIV for Runs 1, 20, and 35 calculated at one of the foot-points of the loop. The intensities are normalized for individual spectra with respect to corresponding maximum intensities. Negative values indicate upward velocity/blueshift.

bulk flow slows down and the temperature and density increase in the foot-point region which starts to emit near the rest wavelength and the line appears enhanced in the blue wing (Figure 1(c)).

When the plasma flows weaken, the spectra once again become Gaussian (Figure 1(d)). Depending on the time interval during which the observational data is gathered, the line would either appear totally blueshifted or stationary Gaussian or blue-/red-wing enhanced. For example, a study by Imada et al. (2008) shows that the distorted Fe XIV line profiles were preferentially observed in new loops just after the impulsive phase whereas symmetric line profiles were observed in old flaring loops after the time of the *GOES* peak flux. Table 1 shows the line parameters for Fe XXIII and XXIV during the time intervals 10–20 s and 8–18 s (Figures 1(c) and 2(c)), respectively, for all 35 runs. The spectra are fitted with the double Gaussian profile. The highest values of μ (mean velocity) of the wing component for Fe XXIII and Fe XXIV are 200.7 and 221.9 km s^{-1} respectively. Milligan & Dennis (2009) records the velocity of 252 $\pm$ 32 and 268 $\pm$ 28 km s^{-1} for the wing component of these lines.

Studies have shown that when asymmetric spectral lines are fitted with double Gaussians, the primary component (line core) shows low speeds whereas the secondary (minor) component shows very high speeds (Bryans et al. 2010; Peter 2010). It is likely that this primary component comprises emission from what we ascribe to low velocity ion populations deeper in the atmosphere whereas, crucially, the secondary component comes from emission from the early high velocity ion populations formed at higher altitudes. This is seen in Figure 4(a) where the 10 s interval is split into two 5 s intervals (i.e., reducing the exposure time of EIS from 10 to 5 s). We see

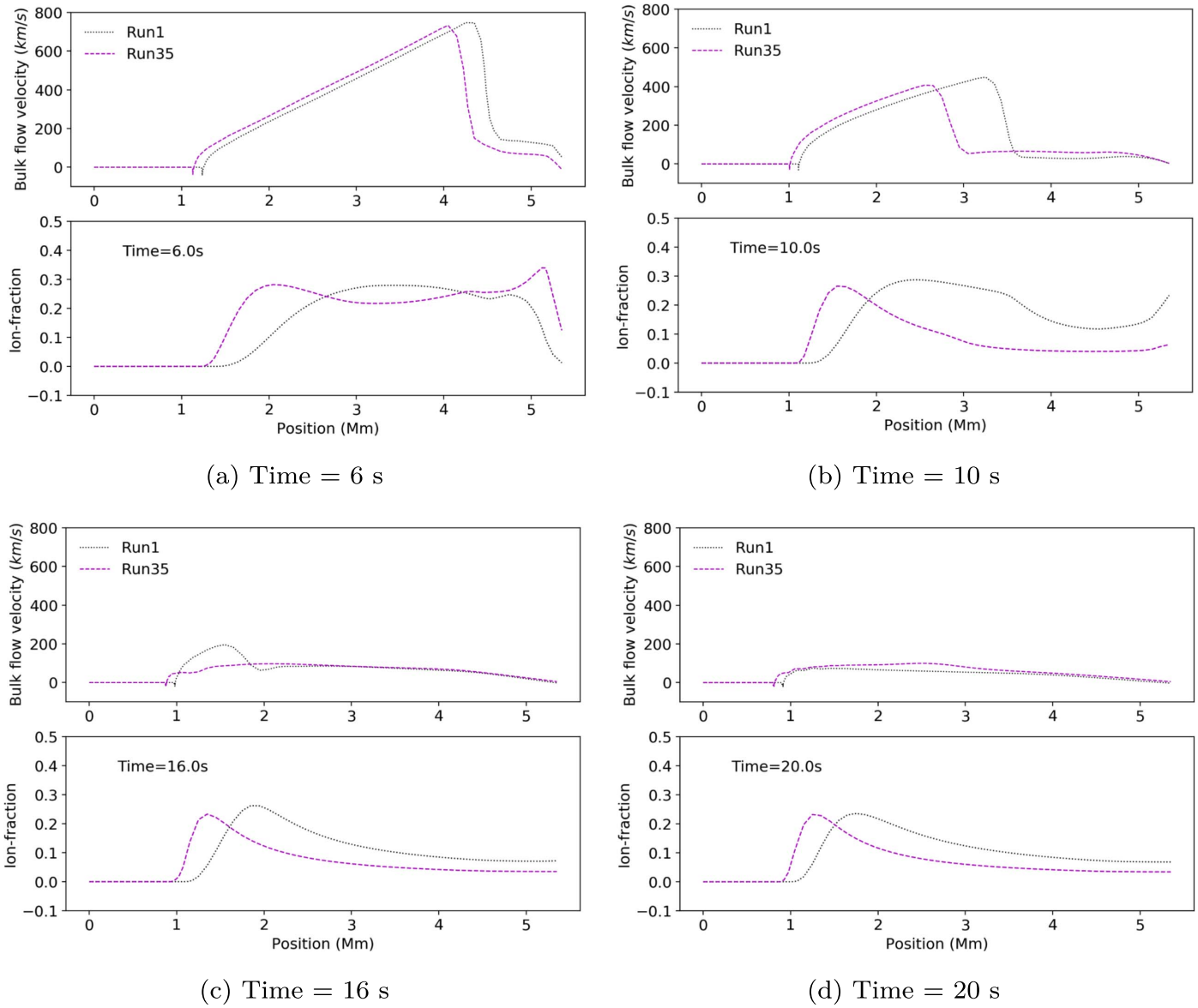

(a) Time = 6 s (b) Time = 10 s

(c) Time = 16 s (d) Time = 20 s

Figure 3. Top panels show bulk velocity while the bottom panels show Fe XXIII ion fraction in each subfigure as a function of position from one foot-point to the apex of the loop at specified times. Positive bulk flow velocities indicate upflows.

that the line that was asymmetric at the 10 s exposure time shows symmetric Gaussian shape during the two subintervals. The secondary component comes from the Gaussian during the 10–15 s interval whereas the primary component comes from the Gaussian during the 15–20 s interval.

The above explanation for asymmetric lines works as long as a detector pixel contains the emission captured from a long column depth. This is generally the case for flare foot-points and the forward modeling code calculates emission by placing the virtual instrument in the plane of the loop and looking directly down on the foot-point. Hence the foot-point pixel contains the emission not just from the foot-point of the loop but from a fairly large region of the loop-leg, whereas pixels near the loop top contain smaller segments of the loop. In a single loop model, we expect to see the wing enhancement from the foot-point pixel but not from the pixels near the loop top when the observing instrument is aligned in this specific way and also due to smaller line-of-sight velocities (Figure 4(b)). However, if the instrument line of sight was perpendicular to the loop plane, there would not be asymmetric lines due to plasma bulk motion simply because the line-of-sight velocity in that case would always be zero. The asymmetries in the lines observed in such alignment of the instrument would be due to reasons other than the bulk motion, e.g., nonthermal effects (Antonucci et al. 1986; Doschek et al. 2014) etc. This highlights the importance of taking into consideration the positioning of the observing instrument with respect to the flaring loop in interpreting the spectra.

3.1. The Role of Loop Length on Spectral Line Shape

Loop length is an important factor that affects plasma dynamics. For example, loop length determines thermal conduction timescale ($\tau_C \propto L^2$) and enthalpy flux timescale ($\tau_V \propto L$) during the cooling phase (Bradshaw & Cargill 2010). To study whether loop length plays an important role in line asymmetry and broadening, we consider five simulations that have different loop lengths but keep the beam parameters the same in each case. The Fe XXIII spectra for each of these runs

Table 1
Fe XXIII and Fe XXIV Line Parameters for All 35 Cases during the Intervals Specified in Figures 1(c) and (g)

#	F, E_c	Fe XXIII				Fe XXIV			
		μ_w	σ_w	μ_c	σ_c	μ_w	σ_w	μ_c	σ_c
1	5, 11	200.5	55.4	64.1	52.6	213.9	57.4	67.4	58.6
2	5, 12	199.7	54.8	64.1	52.7	211.6	56.9	66.9	58.9
3	5, 13	198.0	54.5	65.0	52.7	208.5	56.9	65.6	58.5
4	5, 14	195.2	53.3	68.7	53.9	202.1	56.8	61.7	58.6
5	5, 15	192.6	52.9	59.9	53.9	198.7	56.9	54.1	59.3
6	6, 11	200.7	57.4	66.8	53.2	217.8	59.0	69.7	59.1
7	6, 12	200.4	57.3	67.9	53.2	216.4	58.8	69.4	59.0
8	6, 13	199.3	56.7	68.8	53.2	214.3	58.5	69.2	58.9
9	6, 14	197.7	56.5	64.7	53.6	210.9	58.3	64.4	59.7
10	6, 15	195.1	55.4	68.9	54.5	204.3	58.2	62.1	59.2
11	7, 11	198.7	59.9	70.9	53.4	220.3	60.9	72.2	59.3
12	7, 12	199.7	59.8	70.6	53.7	220.0	60.7	70.5	59.5
13	7, 13	198.8	59.2	70.1	53.7	218.2	60.3	70.4	59.6
14	7, 14	197.2	58.4	70.5	53.9	214.4	59.7	68.5	59.6
15	7, 15	195.8	57.9	68.4	54.3	210.9	59.4	65.4	59.9
16	8, 11	196.4	61.3	68.9	53.9	220.9	62.3	71.1	60.3
17	8, 12	195.9	62.1	73.2	53.7	221.4	62.3	72.9	59.7
18	8, 13	194.6	61.9	74.7	53.6	220.4	62.1	74.2	59.5
19	8, 14	195.0	61.2	74.7	53.9	218.2	61.4	73.1	59.7
20	8, 15	193.2	60.5	75.2	54.5	214.3	60.8	71.0	59.9
21	9, 11	192.0	63.8	70.9	53.9	221.6	64.1	72.3	60.5
22	9, 12	192.4	63.6	72.2	54.0	221.3	63.7	72.9	60.4
23	9, 13	191.3	64.0	74.6	53.9	221.5	63.7	74.3	60.1
24	9, 14	189.5	64.1	77.1	53.8	220.8	63.2	77.4	60.0
25	9, 15	190.9	62.7	67.3	55.4	216.3	62.6	69.0	60.6
26	10, 11	188.0	65.6	71.4	54.2	221.6	65.6	72.4	60.9
27	10, 12	190.0	65.1	69.3	54.5	221.3	65.1	71.7	61.2
28	10, 13	188.7	65.4	67.9	55.3	220.4	65.4	69.8	61.2
29	10, 14	184.5	66.7	77.0	53.9	221.9	64.6	78.7	60.6
30	10, 15	184.9	65.8	70.5	55.2	216.8	64.8	69.5	60.7
31	11, 11	182.4	67.7	68.3	54.9	220.1	67.6	69.9	61.3
32	11, 12	184.7	67.2	68.7	54.9	220.3	66.9	70.8	61.5
33	11, 13	183.3	67.6	70.7	54.5	220.2	66.9	71.7	61.2
34	11, 14	182.0	68.2	73.8	54.1	220.9	66.4	75.1	60.9
35	11, 15	178.1	68.6	75.1	54.3	219.1	65.9	76.5	60.9

Note. Spectra are fitted with double Gaussian (w and c denote wing and core components respectively). F and E_c are in units of $\times 10^{10}$ erg cm^{-2} s^{-1} and keV respectively. μ and σ are in units of km s^{-1}. μ_w and μ_c for both lines are blueshifted (negative velocity).

are shown in Figure 5 during specified time intervals. These time intervals are the intervals during which the line for a particular run showed a blue-wing enhancement. The spectra (including those that showed asymmetry) are fitted with single Gaussian profiles and the resultant line parameters are tabulated in Table 2.

We see that the line shape for the 50 Mm long loop is non-Gaussian with an extended tail in the blue wing during earlier intervals (Figures 5(a) and (b)), whereas spectra for other loops are Gaussian. Second, when the loop is longer, the wing enhancement is seen at later time intervals, e.g., the wing enhancement for the 10.7 Mm loop is seen during the 10–20 s interval whereas for the 20 Mm loop it is seen during the 24–34 s interval. The line intensity for a longer loop is weaker than that of a shorter loop. Another interesting trend we see from Figure 5 and Table 2 is that for a longer loop, the line centroid (μ) is shifted to higher velocities and the line width (as seen from σ) is larger than that for the spectra of shorter loops.

Longer loops have larger radius of curvature and so a greater length falls into the foot-point pixel. Due to this, emission from ions with very extreme velocities is included in the spectrum for long loops. This is the reason for the extended tail in the blue wings for spectra of a long loop (e.g., the spectrum for the 50 Mm loop in Figures 5(a) and (b)). Figures 6 and 7 show the bulk velocity, electron temperature, and Fe XXIII ion density, ion fraction, respectively, as a function of position from a footpoint to the loop top for loops of different loop lengths. Even though each loop is heated with the same beam, the plasma dynamics and ion density/fraction profiles are considerably different, bringing about the differences in the line profiles mentioned above. For a longer loop the amount of plasma is greater since the column depth of plasma is enhanced in longer loops; thus the deposited beam energy lost via radiation is enhanced. This, in addition to the redistribution of heat energy via thermal conduction over a longer loop, makes the foot-point temperature and the overall loop temperature lower compared to that of a shorter loop (Figures 6(b) and (d)). Consequently, the ion density is consistently greater for shorter loops (Figures 7(a) and (c)) as is the line intensity for a shorter loop than for a longer loop ($I \propto n^2$). As the temperature for a longer loop is not only lower but also starts to increase from a location that lies higher up than that of a shorter loop (Figures 6(b) and (d)), the location of maximum ion fraction and density is somewhat higher up in the case of a longer loop

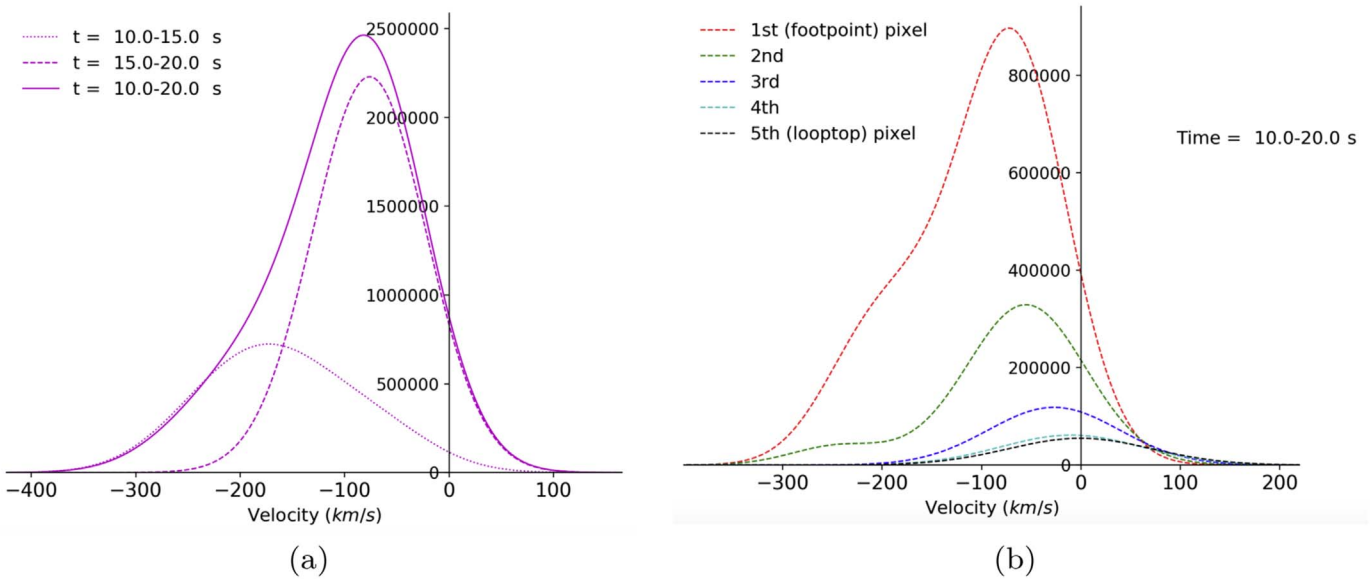

Figure 4. Left: the synthesized Fe XXIII spectra for Run 35 during the time intervals 10–15, 15–20, and 10–20 s to indicate how the spectra would appear if the 10 s exposure time of EIS were reduced to 5 s. Right: Fe XXIII spectral line profiles for Run 10 as seen from different pixels covering different regions of the loop.

(Figure 7). As a result, we see that the line-centroid is shifted to higher velocities for spectra of longer loops (Figure 5). The plasma bulk flow in a longer loop takes a longer time to slow down as the material fronts collide much later for longer loops (Figure 6(c)) and due to the relatively slow increase in the loop temperature a considerable ion population exists in the upper region of the loop for a longer time (Figure 7(d)). Due to these reasons, blue-wing enhancements are observed during later intervals for longer loops than for shorter loops.

It is interesting to note that the line width for longer loops is broader than the line width for shorter loops (see the σ parameter for different loops in Table 2) despite the temperature being lower for the long loops. The only possible explanation for such nonthermal broadening in the present single loop model is a greater line-of-sight column depth and corresponding higher bulk flow speed for longer loops. When the loop is short, the dispersion in the velocity is small since the line-of-sight column depth is short which makes the line width narrow compared to the width for a longer loop. This also explains the positive correlation between the Doppler shift and excess broadening reported by many studies as mentioned in the 1.

It has been observed that the hot Fe lines that are very broad are also symmetric and can be well fitted by a single Gaussian profile (e.g., the Fe XXI spectral line observed by Graham & Cauzzi 2015 and Polito et al. 2016). The modeling study by Polito et al. (2019) concluded that broader profiles observed early on in the simulation are more asymmetric with an extended tail in the blue wing region. The loop length that they used in their multithread model is 100 Mm. As observed above, a longer loop (e.g., the 50 Mm loop) does indeed give the spectrum that is asymmetric with an extended tail (Figures 5(a) and (b)). However, the spectra for shorter loops are broad as well as well fitted with single Gaussian profiles. So it appears that one of the factors that determines whether the symmetric broadening will be observed or not is the loop length and by extension the magnetic geometry. However, the plasma dynamics, bulk flow speeds, and ion density and fraction also depend on the heating parameters. Hence a broader parametric study may reveal the conditions under which the lines are expected to show symmetric broadening.

4. Conclusions

Asymmetries in spectral profiles of hot Fe lines (Fe XXIII, XXIV) were observed during a flare studied by Milligan & Dennis (2009). This flare was modeled using their *RHESSI*-derived beam parameters and corresponding uncertainties by running 35 single loop, field-aligned hydrodynamic simulations. In the flare observations as well as the simulations, only the very hot Fe (XXIII, XXIV) lines showed blue-wing enhancements whereas at cooler temperatures line profiles did not deviate from their Gaussian shape. Additionally the simulations revealed that the spectral profiles of Fe XXIII and XXIV evolved from Gaussian to red-wing enhanced to blue-wing enhanced and back to Gaussian. A detailed analysis of the predicted lines in terms of the plasma bulk flow velocities, ion fractions, and ion densities along the loop offers the following conclusions:

1. The main reason only the hot Fe lines show asymmetries while the lower temperature lines do not is the location over which the populations for these particular ions exist. Since the hot Fe ion populations form over a large portion of the loop, plasma bulk flow velocities at different locations and at different times within the instrument exposure time contribute to the line shape along the line of sight, which is not the case for the cooler ions as they exist mainly in the lower regions of the loop.
2. Initially when the bulk flow speeds are very high, a larger ion population existing in the region above the foot-points leads to the highly blueshifted Gaussian spectrum during early time intervals. As time evolves, the continued heating and slowing of bulk flows causes the ion populations to localize near the foot-points of the loop. This increase in the lower region, low velocity ion populations appears as the red-wing enhancement, and the blue-wing enhancement successively. Once the

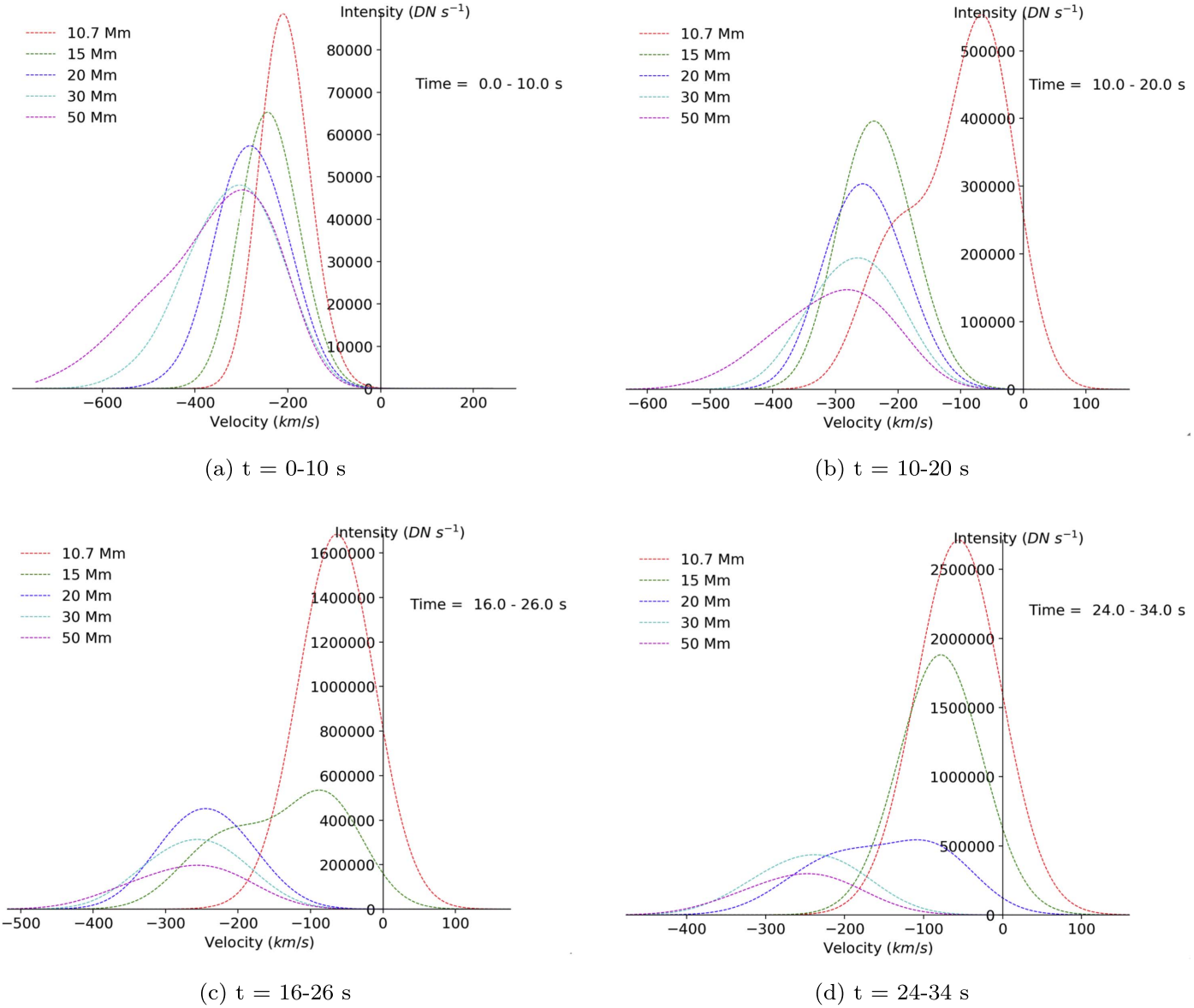

(a) t = 0-10 s

(b) t = 10-20 s

(c) t = 16-26 s

(d) t = 24-34 s

Figure 5. Fe XXIII line spectra at specified time intervals for each run. Negative values indicate upward velocity/blueshift.

Table 2
Fe XXIII Line Parameters when Spectra during Specified Intervals (in Seconds) Are Fitted with a Single Gaussian Profile

$2L$ (Mm)		0–10	10–20	16–26	24–34	40–50
10.7	μ	−207.92	−91.83	−64.18	−55.80	−39.89
	σ	53.60	83.78	53.22	54.28	55.56
15	μ	−240.33	−235.89	−130.30	−78.57	−58.14
	σ	63.74	59.65	96.00	53.10	55.18
20	μ	−278.26	−253.62	−243.75	−146.95	−78.34
	σ	79.87	64.97	65.32	93.63	54.62
30	μ	−314.81	−267.51	−258.19	−242.82	−133.99
	σ	104.76	74.48	70.92	70.90	83.12
50	μ	−338.17	−297.02	−266.67	−253.40	−225.46
	σ	−132.50	−95.96	81.63	73.27	73.93

Note. Blue cells indicate a double-component line while green cells show spectral lines with asymmetric tails in the blue wing (see Figure 5). μ and σ are in units of km s^{-1}. Negative sign indicates upward velocity/blueshift.

plasma flows weaken, the spectrum again becomes Gaussian with a very small Doppler shift.

3. When the spectral lines are synthesized with a smaller exposure time for the observing instrument, e.g., from 10 to 5 s for EIS in this case, the line that showed asymmetry at 10 s exposure time assumes a symmetric Gaussian shape during the corresponding two subintervals, indicating the dynamics happened during two different time intervals.
4. Since the plasma bulk flows at different times and locations along the loop contribute to the asymmetries in spectral lines as shown in this work, the alignment of the observing instrument with respect to the flaring loop needs to be taken into account while explaining spectral asymmetries. Asymmetries observed when the instrument is perpendicular to the loop, e.g., loops near the limb, may be due to reasons other than plasma bulk motion, such as nonthermal effects.

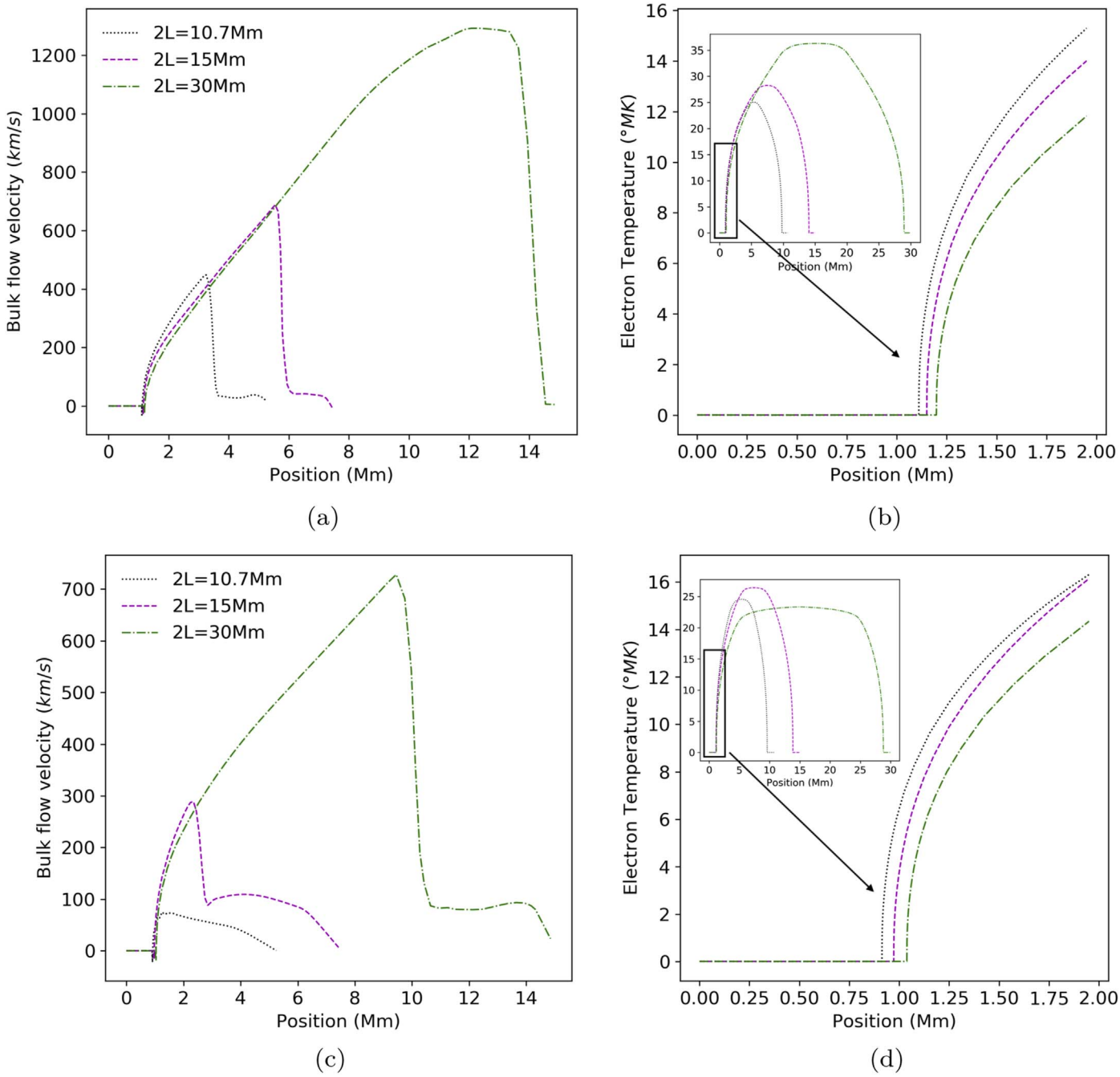

Figure 6. Bulk flow velocity and electron temperature as a function of position from a footpoint to the loop top for runs with $2L = 10.7$, 15, and 30 iMm at 10 s (top) and 20 s (bottom) into the simulations (subfigures (b) and (d) are enlarged to show the differences in the temperature profile near the foot-point region clearly). Positive bulk flow velocities indicate upflows.

To study the role of loop length on line asymmetry and broadening, five simulations with different loop lengths but the same beam parameters were considered. The results offer the following conclusions:

1. For longer loops the line centroid is shifted to higher velocities and the blue wing enhancement is seen at later intervals than for shorter loops.
2. Despite lower temperatures, the line width for longer loops are broader. This excess broadening in long loops is the result of longer line-of-sight column depths which yields a greater velocity dispersion.
3. Loop length is one of the factors that determines whether the broad lines observed very early on during a flare will be symmetric or not. The line-of-sight column depth is longer for longer loops and so emission from very high velocity ions in the upper regions of the loop contributes to the extended tail in the blue wing of the line.

Explaining the observed asymmetric spectral lines is a complex and challenging question that needs consideration of several contributing factors. The work presented here shows that the single loop model can successfully explain many observations regarding line asymmetry and broadening. In particular it confirms the possibility that the line asymmetry

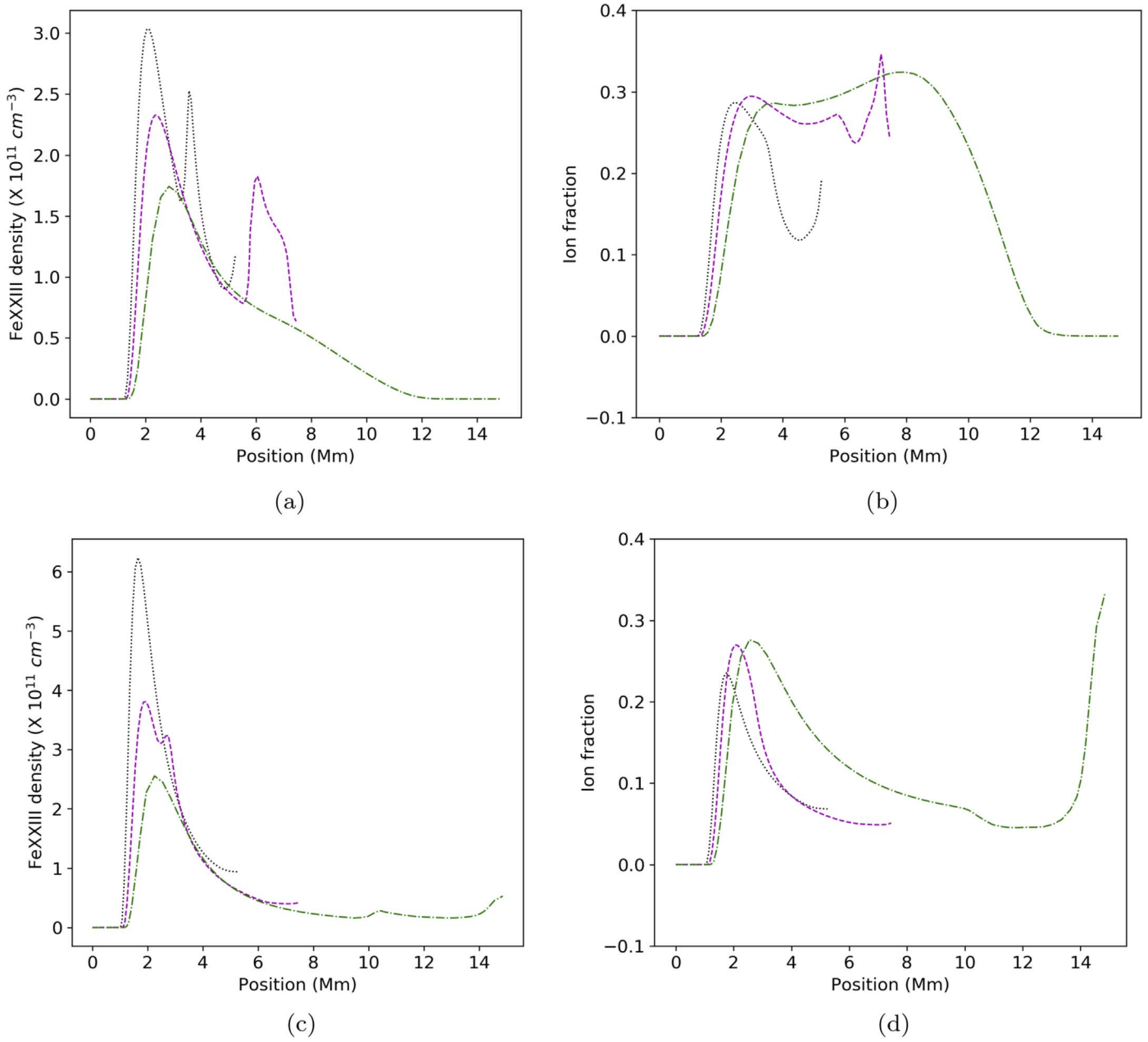

Figure 7. Fe XXIII ion density and ion fraction as a function of position from a footpoint to the loop top for runs with $2L = 10.7$, 15, and 30 Mm at 10 s (top) and 20 s (bottom) into the simulations.

depends on the time resolution of the observing instruments and can also arise due to the early emission from high velocity ions. Moreover, it can be suggested that if a line observed with a sufficiently high cadence instrument (e.g., *IRIS*) is symmetric, then the loop structure may largely be monolithic. However, if the line still shows wing enhancement then that might be an indication of multiple subresolution structures existing in the observed region. Additionally, the time interval during which the wing enhancement is seen also depends on loop length and occurs later for longer loops. The excess broadening is consistent with the line-of-sight velocity dispersion in the plasma bulk flow in a single strand. Moreover, the longer line-of-sight column depths for longer loops lead to stronger velocity dispersion and consequently broader line widths. The longer loops have line centroids shifted to higher velocities as well as broader line widths, giving a positive correlation between the Doppler shifts and excess broadening, as has been observed by several studies. An extended tail in the blue wing is seen when the line is observed very early on in the simulation for the longest loop considered here, whereas the line shows symmetric broadening for the other loops. All these results suggest that loop length plays a very important role in spectral line asymmetry and broadening. Reep & Toriumi (2017) showed that loop length is one of the primary factors that determines the flare timescales such as FWHM and e-folding decay time of the *GOES* light curves. Hence it is crucial to conduct observational studies that will look into the correlation between loop length and excess broadening and wing asymmetry in particular, and other flare characteristics in general.

While this work does not rule out the role of nonthermal physics, non-Gaussian ion distributions, multiple flows,

turbulence, chromospheric spicules, and magnetic perturbations in explaining line asymmetry and broadening, it suggests the importance of ruling out the single loop dynamics explanation first before resorting to complex models or that a simple explanation might be valid in some cases. It is important, however, to note that the explanation presented here works when the line-of-sight dynamics is captured due to the observing instrument being aligned in a specific way. Hence it is necessary to take into account the orientation of the instrument with respect to the flows being observed. Another point to note is that the beam was kept on for the entire duration of the observed impulsive phase (i.e., 360 s). The asymmetric lines were observed at different intervals depending on the loop length, though all within the first 50 s of flare evolution in each case. So if the beam duration is very short or the beam parameters are time dependent then the spectral profiles would be quite different due to the presence of downflows early on. Second, the explanation offered here works only for the very hot Fe lines. However, cooler lines such as Fe XII, XIII, XV, etc., have also been observed to show asymmetry. Hence it is possible that the explanation for asymmetries in these lines may be completely different or the stratification of ion populations (i.e., high speed upper region/low speed lower region) for such ions can be brought about by nonthermal physical processes such as type II spicules or magnetoacoustic waves and/or nonequilibrium effects. This emphasizes the necessity of more studies on spectral line behavior that will thoroughly explore the effects of various key factors on spectral line shape.

The authors were funded for this work by the Heliophysics Supporting Research (H-SR) element of NASA ROSES (grant NNX17AD31G). The authors thank the anonymous referee for constructive comments.

ORCID iDs

Revati S. Mandage https://orcid.org/0000-0002-8084-5921
Stephen J. Bradshaw https://orcid.org/0000-0002-3300-6041

References

Alexander, D. 1990, A&A, 236, L9
Antonucci, E., Rosner, R., & Tsinganos, K. 1986, ApJ, 301, 975
Battaglia, M., Kleint, L., Krucker, S., & Graham, D. 2015, ApJ, 813, 113
Bradshaw, S. J. 2009, A&A, 502, 409
Bradshaw, S. J., & Cargill, P. J. 2010, ApJ, 717, 163
Bradshaw, S. J., & Cargill, P. J. 2013, ApJ, 770, 12
Bradshaw, S. J., Del Zanna, G., & Mason, H. E. 2004, A&A, 425, 287
Bradshaw, S. J., & Klimchuk, J. A. 2011, ApJS, 194, 26
Bradshaw, S. J., & Klimchuk, J. A. 2015, ApJ, 811, 129
Brosius, J. W. 2003, ApJ, 586, 1417
Bryans, P., Young, P. R., & Doschek, G. A. 2010, ApJ, 715, 1012
Carlsson, M., & Leenaarts, J. 2012, A&A, 539, A39
Culhane, J. L., Harra, L. K., James, A. M., et al. 2007, SoPh, 243, 19
De Jager, C. 1985, SoPh, 98, 267
De Pontieu, B., Title, A. M., Lemen, J. R., et al. 2014, SoPh, 289, 2733
Dere, K. P., Bartoe, J. D. F., & Brueckner, G. E. 1989, SoPh, 123, 41
Doschek, G. A., Antiochos, S. K., Antonucci, E., et al. 1986, in Energetic Phenomenon on the Sun: The Solar Maximum Mission Flare Workshop, ed. M. R. Kundu & B. Woodgate (Greenbelt, MD: NASA Goddard Space Flight Center), 87N19334
Doschek, G. A., Kreplin, R. W., & Feldman, U. 1979, ApJL, 233, L157
Doschek, G. A., Mariska, J. T., & Sakao, T. 1996, ApJ, 459, 823
Doschek, G. A., Mariska, J. T., Warren, H. P., et al. 2007, PASJ, 59, S707
Doschek, G. A., McKenzie, D. E., & Warren, H. P. 2014, ApJ, 788, 26
Doschek, G. A., Warren, H. P., Dennis, B. R., Reep, J. W., & Caspi, A. 2015, ApJ, 813, 32
Doschek, G. A., Warren, H. P., Mariska, J. T., et al. 2008, ApJ, 686, 1362
Dudík, J., Polito, V., Janvier, M., et al. 2016, ApJ, 823, 41
Fletcher, L., & Hudson, H. S. 2008, ApJ, 675, 1645
Graham, D. R., & Cauzzi, G. 2015, ApJL, 807, L22
Hara, H., Nishino, Y., Ichimoto, K., & Delaboudinière, J.-P. 2006, ApJ, 648, 712
Harrison, R. A., Sawyer, E. C., Carter, M. K., et al. 1995, SoPh, 162, 233
Imada, S., Hara, H., Watanabe, T., et al. 2008, ApJL, 679, L155
Jeffrey, N. L. S., Fletcher, L., & Labrosse, N. 2016, A&A, 590, A99
Jeffrey, N. L. S., Fletcher, L., & Labrosse, N. 2017, ApJ, 836, 35
Klimchuk, J. A., & Bradshaw, S. J. 2014, ApJ, 791, 60
Larosa, T. N., & Moore, R. L. 1993, ApJ, 418, 912
Li, Y., & Ding, M. D. 2011, ApJ, 727, 98
Mason, H. E., Shine, R. A., Gurman, J. B., & Harrison, R. A. 1986, ApJ, 309, 435
Milligan, R. O. 2011, ApJ, 740, 70
Milligan, R. O. 2015, SoPh, 290, 3399
Milligan, R. O., & Dennis, B. R. 2009, ApJ, 699, 968
Orrall, F. Q., & Zirker, J. B. 1961, ApJ, 134, 72
Patsourakos, S., & Klimchuk, J. A. 2006, ApJ, 647, 1452
Peter, H. 2010, A&A, 521, A51
Polito, V., Dudík, J., Kašparová, J., et al. 2018, ApJ, 864, 63
Polito, V., Reep, J. W., Reeves, K. K., et al. 2016, ApJ, 816, 89
Polito, V., Reeves, K. K., Zanna, G. D., Golub, L., & Mason, H. E. 2015, ApJ, 803, 84
Polito, V., Testa, P., & Pontieu, B. D. 2019, ApJL, 879, L17
Polito, V., Zanna, G. D., Valori, G., et al. 2017, A&A, 601, A39
Pontieu, B. D., McIntosh, S. W., Hansteen, V. H., & Schrijver, C. J. 2009, ApJ, 701, 6
Reep, J. W., Bradshaw, S. J., Crump, N. A., & Warren, H. P. 2019, ApJ, 871, 18
Reep, J. W., Bradshaw, S. J., & Holman, G. D. 2016, ApJ, 818, 44
Reep, J. W., Bradshaw, S. J., & McAteer, R. T. J. 2013, ApJ, 778, 76
Reep, J. W., & Toriumi, S. 2017, ApJ, 851, 4
Tian, H., Li, G., Reeves, K. K., et al. 2014, ApJL, 797, L14
Vernazza, J. E., Avrett, E. H., & Loeser, R. 1981, ApJS, 45, 635
Watanabe, T., Hara, H., Sterling, A. C., & Harra, L. K. 2010, ApJ, 719, 213
Young, P. R., Doschek, G. A., Warren, H. P., & Hara, H. 2013, ApJ, 766, 127
Young, P. R., Tian, H., & Jaeggli, S. 2015, ApJ, 799, 218
Zanna, G. D., Mitra-Kraev, U., Bradshaw, S. J., Mason, H. E., & Asai, A. 2011, A&A, 526, A1